

Strain-induced magma degassing: insights from simple-shear experiments on bubble bearing melts

Luca Caricchi, Anne Pommier, M. Pistone, Jonathan M. Castro, Alain Burgisser, D. Perugini

▶ **To cite this version:**

Luca Caricchi, Anne Pommier, M. Pistone, Jonathan M. Castro, Alain Burgisser, et al.. Strain-induced magma degassing: insights from simple-shear experiments on bubble bearing melts. Bulletin of Volcanology, 2011, 73 (9), pp.1245-1257. 10.1007/s00445-011-0471-2 . insu-00597312

HAL Id: insu-00597312
https://insu.hal.science/insu-00597312

Submitted on 23 Jun 2011

HAL is a multi-disciplinary open access archive for the deposit and dissemination of scientific research documents, whether they are published or not. The documents may come from teaching and research institutions in France or abroad, or from public or private research centers.

L'archive ouverte pluridisciplinaire **HAL**, est destinée au dépôt et à la diffusion de documents scientifiques de niveau recherche, publiés ou non, émanant des établissements d'enseignement et de recherche français ou étrangers, des laboratoires publics ou privés.

Strain-induced magma degassing: Insights from simple shear experiments on bubble bearing melts

Luca Caricchi[1,2], Anne Pommier[2, 3], Mattia Pistone[4], Jonathan Castro[2,5], Alain Burgisser[2], Diego Perugini[6]

1) Department of Earth Sciences, University of Bristol, Wills Memorial Building, Queens's Road, Bristol BS8 1RJ, United Kingdom.
2) Centre National de la Recherche Scientifique (CNRS), Institut National des Sciences de l'Univers (INSU), Université d'Orléans, Université François Rabelais–Tours, Institut des Sciences de la Terre d'Orléans, UMR 6113, Campus Géosciences, 1A, Rue de la Férollerie, 41071 Orléans cedex 2, France.
3) Massachusetts Institute of Technology, Department of Earth, Atmospheric and Planetary Sciences, 32 Vassar Street, 54-1224, 77 Massachusetts Avenue, Cambridge, MA 02139, USA
4) Department of Earth Sciences, ETH Zurich, Clausiusstrasse 25, 8092 Zurich, Switzerland
5) School of Geosciences, Monash University, Victoria 3800, Australia.
6) University of Perugia, Department of Earth Sciences, Piazza Università 1, 06100, Perugia, Italy.

Corresponding author:

Luca Caricchi

NERC Fellow

Department of Earth Sciences, University of Bristol

Wills Memorial Building, Queen's Road, Bristol BS8 1RJ, United Kingdom

e-mail: l.caricchi@bristol.ac.uk; phone: +44 117 331 51 58; fax: +44 117 925 33 85

Abstract

Experiments have been performed to determine the effect of deformation on degassing of bubble bearing melts. Cylindrical specimens of phonolitic composition, initial water content of 1.5 wt.% and 2 vol.% bubbles, have been deformed in simple

shear (torsional configuration) in an internally heated Paterson-type pressure vessel at temperature of 798-848 K, 100-180 MPa confining pressure and different final strains. Micro-structural analyses of the samples before and after deformation have been performed in two and three dimensions using optical microscopy, a nanotomographer and synchrotron tomography. The water content of the glasses before and after deformation has been measured using Fourier Transform Infrared Spectroscopy (FTIR). Up to a total applied strain of $\gamma \sim 2$ the bubbles record accurately the applied strain, whereas at higher strains ($\gamma \sim 10$) the vesicles become very flattened and elongated in the direction of shear. The residual water content of the glasses remains constant up to a strain of $\gamma \sim 2$ and decreases to about 0.2 wt.% at $\gamma \sim 10$. Results show that strain enhances bubble coalescence and degassing even at low bubble volume fraction. Noticeably, deformation produced a strongly water under-saturated melt. This suggests that degassing may occur at great depths in the volcanic conduit and may force the magma to become super-cooled early during ascent to the Earth surface potentially contributing to the genesis of obsidian.

Keywords: Magma deformation, strain-induced degassing, bubble deformation, obsidian banding.

Introduction

The style and rate of degassing during magma ascent in volcanic conduits is one of the main factors controlling eruption dynamics. As an example, the transition from highly explosive to effusive eruptions, as recently observed at Chaitén volcano (Chile; Castro and Dingwell, 2009), may result from the efficient degassing of high viscosity magmas through a permeable bubble network. Magma experiences large shear deformation along conduit walls during ascent to the surface, a process that has

been proven to strongly enhance bubble coalescence and favour magma degassing (Rust et al., 2003; Okumura et al., 2008; Okumura et al., 2009). Previous experimental studies carefully investigated the effect of strain and bubble content on connectivity showing that long-range bubble connectivity increases as strain and bubble volume fraction increase (Okumura et al., 2008; Okumura et al., 2009). The achievement of a connected network of bubbles may provide pathways for the gas to migrate through the magmatic mass, thus enhancing significantly magma degassing. Although a number of works shed new light on the possible processes associated with magma degassing, there are still open questions about the mechanisms responsible for removal of the gas phase from magma bodies (e.g. Yoshimura and Nakamura, 2008). In particular while it is intuitive that a connected network of bubbles would favour degassing, it is not clear which process may act to preserve this network open for sufficient time span to release a significant amount of gas from the magma. Yoshimura and Nakamura (2008) envisage that the transfer of gas from melt to an interconnected degassing path is mainly controlled by H_2O diffusion in the melt phase, which, in turn, is controlled by water concentration gradient and the pressure difference between the connected gas path and the magma. As a result, diffusive degassing requires significant durations (hundreds of hours; Yoshimura and Nakamura, 2008) to explain the formation of degassed and bubble-free bands (2-3 mm in thickness) observed in obsidians (Castro et al., 2005). Other processes occurring over shorter timescales should therefore play an active role in the degassing history of ascending magmas.

Here we experimentally investigate how strain/deformation induces and enhances the transfer of gas from a magma having only a modest quantity (<5%) of bubbles and at pressure conditions appropriate for magma in the deep plumbing

system (4-6 km). This contrasts with previous studies that investigated the loss of gas from magmas with relatively high volume fraction of bubbles (e.g. Burgisser and Gardner, 2005; Okumura et al., 2008). Focusing on magmas containing small amounts of bubbles is fundamental to constraining the maximum depth at which degassing can play a role in the dynamics of volcanic eruptions. The potential applicability of our results to better understand the genesis of obsidians is also discussed.

Experimental techniques

Synthesis of starting material

Pumices from the 3760 BP Avellino eruption (Rolandi et al., 1993) were finely ground and cold pressed in large volume stainless steel canisters (36 mm external diameter, 34 mm internal diameter and ca. 100 mm in length). The fine powders obtained from the pumices were isostatically pressed at 180 MPa and 1373 K in an internally heated pressure vessel (pressurized with Argon, 40 litres of heated volume). Temperature was held constant for 24 hours. Samples were cooled with a rate of about 60 K/min to 753 K; the cooling rate was subsequently decreased to 0.6 K/min down to room temperature. This procedure generated a crystal free glass while avoiding the formation of cooling cracks. The gas content of pumices, before the synthesis, was determined to be 2.44 wt.% by loss on ignition. This value is in agreement with the study of Signorelli et al. (1999), in which the relative content of Cl, F, S and H_2O was measured on the same rock used as starting material for our experiments. The water content of the glass after the synthesis, measured by FTIR, was 1.5±0.16 wt.%. The glass was imaged by 3D tomography and the bubble content was ca. 2 vol.%. At the pressure and temperature conditions of the synthesis, the silicate melt is undersaturated in volatiles (Moore et al., 1998; Signorelli et al., 1999).

During cooling, the pressure decreased at about ~1.3 MPa/min while the sample temperature remained comparatively high and constant due to the dimension of the specimen. Water vesicles were thus likely generated upon cooling. The presence of some residual air in the canisters and its limited solubility in silicate melts (Mysen et al., 2008) contributed to the nucleation and stabilization of the water vesicles. The gas bubbles present in the samples thus contain a mixture of air and water; the small volume fraction of bubbles makes the starting material suitable for the present experimental study.

(FIGURE 1)

Simple shear deformation experiments

Experiments were performed in a Paterson-type deformation apparatus in torsion configuration, which imposes a simple shear strain field (Paterson and Olgaard, 2000; Fig. 1A), at temperatures of 823 and 873 K and confining pressures of 100 and 180 MPa. In this configuration, the strain increases linearly from the centre to the outer portions of the samples (Paterson and Olgaard, 2000). Cylindrical specimens of 15 mm diameter and 10 mm length were drilled out from the canisters used for the synthesis. Samples were placed in the centre of a symmetrical assembly, of the same diameter of the specimen, comprised on both sides by an alumina disk (3 mm length), an alumina cylinder (50 mm length) and a zirconia stabilized ceramic cylinder (30 mm length; Fig. 1A). The experimental assembly was inserted in pure iron or copper tube (jacket; 250 μm wall thickness) for the experiments performed at 180 and 100 MPa respectively. Metallic jackets separate the sample from contact with the Argon gas, used as confining medium. The furnace was previously calibrated and maximum temperature variations of about 2 K were allowed along the sample length. The ceramics constituting the top part of the assembly, except for the disk in contact with

the sample, were hollow and the central hole hosted a thermocouple used for temperature measurements. The thermocouple was connected to atmospheric pressure and consequently the hole was at 0.1 MPa during the runs. The surfaces of ceramic surrounding the sample were slightly rough, which allowed the gas released by the sample to flow between the metallic jacket and the ceramic disk and escape through the thermocouple hole (Fig. 1A and B). An additional degassing path was present in the core of the specimens where a cylindrical electrode for electrical conductivity measurements was placed, as explained in the following section. As such, this experimental configuration allowed us to study the effect of deformation on degassing.

Electrical conductivity measurements

Impedance measurements were planned and for this purpose the core of the specimens was drilled to host a 4 mm diameter cylinder of copper (Fig. 1A). Unfortunately, the transmission of the electrical signal between the Impedance Gain Phase Analyzer was not continuous during the experiments, precluding a straightforward interpretation of the electrical response of the samples. The central electrode was nevertheless employed in all the experiments to maintain the same geometrical setup.

Analytical techniques (TABLE 1)

The chemical composition of the natural samples used to synthesize the starting material was analysed by X-Ray Fluorescence (XRF; Table 1) at the institute of Mineralogy and Petrology of ETH Zurich (Switzerland). The composition of the samples after the experiments was analyzed using a JEOL-JXA-8200 Electron Microprobe Analyzer (EMPA; Table 1) at ETH Zurich (Switzerland). EMPA analytical conditions were 15 kV acceleration voltage, 5 nA beam current and 15 μm

beam diameter. Negligible compositional differences were detected before (XRF) and after (EMPA) the experiments (Table 1).

Fourier Transform Infrared Spectroscopy (FTIR)

The water content of glasses was measured by a Nicolet Magna 760 instrument connected to a Nic-Plan microscope (Gaillard et al., 2001). A globar SiC source, a MTC/A detector and a CaF_2 splitter were used for the measurements. Spectra were collected between 2000 and 7400 cm^{-1} with a 4 or 8 cm^{-1} resolution. Measurements were acquired on a minimum of 5 points (spot size 80-100 μm) for each sample from the core to the outer portion of the specimens. Absorption coefficient for the 4470 cm^{-1} and 5210 cm^{-1} bands, and densities from Marziano et al. (2007) were used to obtain the total water content from the FTIR spectra. Bubble spacing in the different samples (150-400 μm) was sufficient to allow for accurate measurement of the matrix glass.

X-ray tomography (TABLE 2)

Cylindrical cores of 2 mm outer diameter and lengths between 2 and 4 mm were drilled out from the starting glass and from the deformed samples. Tomographic scans of the experiment performed at the highest strain (γ =9.6) were acquired from a larger section of the sample (~7 mm by ~6 mm by ~3 mm). The longest side of the section was cut along the sample radius and, consequently, the applied strain increases towards the external portion (Paterson and Olgaard, 2000).

Three-dimensional images were acquired using a Phoenix Nanotom 180 X-ray Nanotomograph (for samples PP117 int., Table 2) at the Institute of Earth Sciences of the University of Orleans (France) and at the TOMCAT beamline (for sample PP116, PP117, and starting material, Table 2; Stampanoni et al., 2006) at the Swiss Light Source (Paul Scherrer Institut, Villigen, Switzerland).

Micro-tomography analyses were performed with the Phoenix Nanotom 180 by mounting the specimens on a carbon fibre rod with a thermoplastic adhesive. Samples were placed in the chamber and rotated by 360 degrees during acquisition. An operating voltage of 70 KeV and a filament current of 220 nA were applied. The distance between the sample and the X-ray source and between the X-ray source and the detector was 11.5 and 280 mm, respectively. 2400 2D images were acquired during sample rotation with a resolution of 2.05 μm per voxel (i.e. the smallest volume element of the regular grid in the 3D space). The 2D raw images were converted into 3D image stacks using a micro-cluster of four Personal Computers with the Phoenix 3D reconstruction software.

At the TOMCAT beamline 2001, raw projections were acquired for each scan with 20 KeV energy using a 10x magnification objective and an exposure time of 100 ms. For each scan 32 dark and 451 flat images were collected, thus substantially improving the signal to noise ratio. A LAG Ce 20 μm scintillator was used to convert X-ray photons to visible light, which was projected on a 14bit-CCD camera. The result was a 2048x2048 pixel image for each projection with a resolution of 0.75 μm per voxel. The ImageJ software was used to reduce noise in the tomographic image stacks and to convert them to binary format. The 3D visualization and analysis of the gas vesicles was performed using the open source software Paraview (http://www.paraview.org/) and Blob3D (Ketcham, 2005), respectively.

We converted the reconstructed, grayscale image stacks to binary format with Image J software. We first applied an anisotropic diffusion filter to each image in the stack, thereby eliminating small (1-2 pixel) isolated noise. Thresholding was then performed by manually adjusting the threshold cutoff point on a grayscale value histogram (i.e. the grayscale threshold dividing pixels into either white and black

color) whilst observing that the integrity of the bubble-glass margins, bubble shapes, and bubble walls was maintained as adjustments were made. Because the grey scale contrast between the voids (bubbles) and matrix (glass) is quite large, this procedure resulted in minimal degradation of bubble shapes and sizes. We estimate that errors associated with binarization of bubble size and connectivity are lower than 5% of the measured values.

The two analytical facilities were used according to availability. The TOMCAT scans were acquired at the SLS synchrotron for which a limited amount of time is assigned for each experiment. The availability of an in-house tomography apparatus in Orleans made possible the completion of the additional required scans.

(FIGURE 2)

Results

Although experiments were performed below liquidus temperature, no crystallization occurred because of the short duration of the experiments. In all the experiments an initial elastic response, represented by a steep increase of stress upon the application of the strain rate, was followed by a strain hardening stage (yielding) and flow at relatively constant stress (Fig. 2 A and B). A correction for the presence of the metallic jacket was applied using calibration measurements that characterized the shear strength of the metallic jacket at the same temperature and pressure range as that of the experiments.

Significant stress and temperature oscillations were observed during deformation at 100 MPa, whereas both the recorded signals were constant during the experiments at 180 MPa (Fig. 2).

180 MPa confining pressure and iron jacket

A pilot experiment (PP097) was performed at different temperatures and applied strain rates to explore the rheological behaviour of the sample over a wide range of conditions. Temperature was varied between 798-848 K and the shear strain rate was increased from $1 \cdot 10^{-5}$ to $1 \cdot 10^{-4}$ s^{-1} (Fig. 2; Table 2). A second experiment (PP098) was carried out at constant temperature (848 K) while performing three strain rate steps from $5 \cdot 10^{-5}$ to $3 \cdot 10^{-4}$ s^{-1} (Fig. 2, Table 2). The stress increased for increasing strain rate although the apparent viscosity (stress/strain rate ratio) decreased of about 7% as deformation rate increased. Experiment PP098 also showed some additional shear hardening (increase of stress with increasing strain) for strain larger than 0.5 (Fig.2A). Inspection of this sample after deformation highlighted the presence of marked wrinkles on the metallic jacket (see inset in Fig. 2A), testifying for a marked strength difference between the sample and the iron jacket. The occurrence of wrinkles was responsible for the observed shear hardening. As a result, the possible influence of the metallic jacket on the rheological behaviour of sample PP098 deformed at 848 K precludes the possibility of interpreting the observed decrease of viscosity with increasing strain rate as an expression of non-Newtonian behaviour of the sample. Aiming to reduce the strength contrast between the sample and the metallic jacket, we performed the rest of experiments using copper jackets around the experimental assembly.

100 MPa confining pressure and copper jacket

Experiments PP116 and PP117 were performed at constant temperature (823 K) and at the lower confining pressure of 100 MPa. No wrinkles on the metallic jacket were observed with this new experimental configuration. Large stress instabilities (up to about 4 MPa) were observed in both experiments and were associated with significant variations in the temperature (up to 6 K) recorded by the thermocouple

atop the specimens (Fig. 2 C and D). A closer investigation of the relationship between stress and temperature instabilities revealed that the oscillation of stress and temperature were out of phase by about 90° (i.e. a minimum in stress corresponded to a peak in temperature; Fig. 2 C and D).

In general, these two experiments gave similar apparent viscosities, which suggest sample homogeneity (Table 2). This supports the view that the relatively high viscosities measured at 848K in PP097 and PP098 were probably related to the use of an iron jacket, which gave less accurate rheological results because of higher strength of this metal with respect to the sample. Both the relatively small range of strain rates applied to the specimens and the significant variations of stress recorded during the experiments did not permit an accurate determination of the rheological behaviour of the material as function of applied strain rates. These experiments did, however, given indications on the rheological evolution of bubble-bearing melts with increasing deformation.

(FIGURES 3 AND 4)

X-ray tomography and bubble analysis

Analyses of the 3D volumes reconstructed by X-ray tomography evidenced a number of changes associated with the deformation of bubble-bearing samples. Increasing applied strain resulted in a change of bubble shapes from spherical to ellipsoidal and finally planar at γ of 9.6 (Figs. 3 and 4).

Figure 3 displays the volume reconstruction for a sample that did not experience deformation (i.e. the starting material, A) and a sample in which total applied strain was 1.6 (B). Volumes for each bubble were measured by Blob3D software and the resulting vesicle size distributions are presented in Figure 5. Vesicle sizes correspond to the equivalent radius (radius of a sphere with the same volume as

the object under consideration), and 4 stages of deformation are shown: γ 0, 1.6, 5.5, and 9.6. Data for γ 5.5 were obtained by analysing an additional section of experiment PP117 closer to the core where the applied strain is lower (Paterson and Olgaard, 2000).

(FIGURE 5)

The 3D analyses indicate that deformation produced a general increase of bubble flattening (Figs. 3, 4). Figure 5 shows the appearance of a population of larger bubbles already at γ 1.6. Increasing γ to 5.5 results in the generation of a large population of bubbles with relatively small volume, most likely associated with bubble breakage during deformation. At the highest strain the presence of bubbles with large equivalent radius (i.e. large volume) suggest strain induced bubble coalescence. This is in agreement with the observation of Okumura and co-authors (2008), which suggested that deformation promotes bubble coalescence.

The total volume of bubbles decreases only slightly with deformation (from about 2 to 1.5 vol.% at the highest total γ).

(FIGURE 6)

Water content analyses

FTIR analyses were performed on the glass before and after deformation from the inner to the outer portions of the samples. The initial water content and water content at strain = 1.6 are the same within error; however, the water content at strain = 9.6 is significantly lower, at 0.2 wt.% (Fig. 6). Analyses of water content in a static experiment (PP144), performed with the same experimental setup and duration as PP117, gave the same water content as the starting material, suggesting that deformation was responsible for the loss of water.

Discussion

Experimental results provided information on the effect of bubble deformation on the viscosity of bubbly magmas and also on the influence of deformation on degassing.

(FIGURE 7)

Rheology and strain localization

Viscosities measured for the bubble bearing melts were compared with those of a bubble-free melt with the same composition (Giordano et al., 2008; Fig. 7). Results indicate that the measured viscosity at the lowest temperature and strain rate of $3 \cdot 10^{-5}$ s^{-1} is close to that of the bubble-free system (Fig. 7). On the contrary, at the highest temperature (848 K) the measured viscosities are always higher than those of the bubble free melt. This is likely related to the high resistance to deformation of the iron jacket used in the experiments, which masked the rheological properties of the sample.

The experiments performed at 823K with copper jacket are characterized by large oscillations of stress and the temperature recorded by the thermocouple with increasing strain (Fig. 2), with a minimum measured viscosity that is about one order of magnitude lower than the viscosity of the pure melt (Fig. 7). To quantify the influence of bubbles on the rheology of these samples, it is fundamental to characterize the behaviour of the gas bubbles during deformation. The bubble relaxation time (λ) is a measure of the timescale over which a bubble can respond to changes in its shear environment (Llewellin et al., 2002):

$$\lambda = \frac{r \eta_s}{\Gamma} \qquad (1)$$

where r is the radius of the bubble, η_s is the shear viscosity and Γ is the surface tension. For an average bubble radius of 9 μm (Figure 5), a surface tension between the gas and the melt of 0.25 Nm^{-1} (Llewellin and Manga, 2005) and melt viscosity at

823 K of $10^{10.7}$ Pa·s; (Giordano et al., 2008), λ is higher than 500 hours. In our experiments, the deformation times are much shorter than the relaxation time. The effect of surface tension between gas and bubble is thus negligible and the bubbles behave as passive tracer of shear (i.e. increasing deformation in simple shear induces flattening). Under such conditions, the viscosity of the diluted bubble-bearing melt can be calculated by effective medium theory (Hashin and Shtrikman, 1962; Manga and Loewenberg, 2001; Costa et al., 2009), and the viscosity of the system is fundamentally controlled by the arrangement of the bubbles in the melt. If the bubbles are isolated and do not interact, and the viscosity of the gas (η_g) is approximated to zero (η_g=6·10^{-5} Pa·s at 823 K and 100 MPa; IAPWS, 1997), the viscosity of the system as function of the gas fraction is given by (η_{HS+}; Hashin and Shtrikman upper bound; Costa et al., 2009; Manga and Loewenberg, 2001; Hashin and Shtrikman, 1962):

$$\eta_{HS+} = \eta_m\left(1-\frac{5\phi}{3+2\phi}\right) \qquad (2)$$

where η_m is the melt viscosity (from Giordano et al., 2008), and ϕ_g is the volume fraction of bubbles (Fig. 7). Figure 7 shows that the minimum viscosity measured during the experiments is much lower than expected for a material containing 2 vol.% of isolated bubbles (Eq. 2). An additional deformation mechanism is therefore required to account for such a difference. With increasing strain, bubbles did not simply become more elongated but also extremely flattened and their volume increased (Figs. 3-5). Strain-induced coalescence is most likely responsible for the increase of the volume of the bubbles. The combination of such coalescence with the extremely flattened shape of the bubbles results in the generation of planar, gas-rich structures in the sample. Small local variations of bubble fraction could result in strain

localization in portions of the sample where the bubble content is higher. Since strain localization favours additional coalescence, the resulting pattern quickly becomes extended planar structures where additional localization occurs. The presence of such gas-rich planes where the strain localises could induce a substantial decrease of the bulk viscosity of the sample and account for the relatively low viscosity observed in our experiments.

The effect of such localisation could be even stronger since the calculations presented in Figure 7 do not take into account water loss from the melt and the related increase of viscosity induced by degassing. The loss of about 1.4 wt.% water (experiment PP117), at constant temperature of 823 K, would result in a 5 orders of magnitude increase of melt viscosity (Giordano et al., 2008). This would imply a significant contribution of strain localization to the bulk viscosity of the samples.

(FIGURE 8)

During deformation experiments, the measured viscosity varied continuously (Fig. 2B), reflecting variations in the volumetric fraction of sample affected by shear localization. An inverse correlation was present between these oscillations in viscosity and the increase of temperature recorded by the thermocouple (Figs. 2 C, D). A possible explanation for this occurrence is that coalescence and shear localization may have culminated in the formation of a gas network connected to the thermocouple hole pressurized at 0.1 MPa (Fig. 1B). In this respect, localization of strain on one or more gas layer/s could account for the minimum reached in the applied shear stress and the coincident maximum in temperature should reflect the passage of gas through the thermocouple hole (Figs. 2C, D and 8). This is consistent with the fact that at 100 MPa and temperature of 823K the gas (N_2-O_2-H_2O; see starting material paragraph) is

likely above the Joule inversion temperature and consequently an expansion produces heating of the gas phase (IAPWS, 1997).

To summarize, small local variations of bubble fraction are the likely cause of strain localization, which, in turn increases local strain and favours bubble coalescence. Under the unsteady flow conditions prevailing in our experiments, the vesicles tend to flatten with increasing deformation and generate low viscosity planar features on which the strain localises further. This positive feedback mechanism could be amplified by the local increase of temperature due to viscous heating (Hess et al., 2008). The positive feedback enhancing strain localization can only be ceased if a gas network is established and it connects to a lower pressure region. In this case, the gas is extracted and the bubble fraction decreases, causing a local increase of viscosity that could potentially lead to strain localization in another portion of the material.

Strain-induced degassing

The experiments demonstrate that deformation is responsible for the loss of gas from bubble-bearing melts. The deformation and coalescence of the vesicles with increasing applied strain may result in the generation of extended degassing paths, which increase the melt interface exposed to degassing. Additionally, the stretching of the bubbles associated to deformation reduces the thickness of the diffusive boundary layer increasing the concentration gradient present at the melt-gas interface, which in turn, increases the degassing flux into the connected bubble network (e.g. Lensky et al., 2001). This process increases the concentration gradient of the volatiles diffusing into the vesicles, accelerating the degassing process. The loss of water should induce a strong increase of the melt viscosity (Giordano et al., 2008). In our case, however, it was only slightly recorded (see the general increase of applied stress in Fig. 2B) in the experiment performed to a total strain of γ 9.6, because of the counteracting effect of

shear localization on gas planes. The oscillations of stress and temperature recorded by the thermocouple suggest that degassing occurred cyclically (Fig. 2). The very low decrease of total bubble fraction with increasing deformation suggests, however, that residual bubbles remained in the melt once the connected bubble path sealed (Fig. 8). This is in agreement with the fact that isolated, residual bubbles can only be closed once the gas present in the vesicles diffuses back to the melt (Yoshimura and Nakamura, 2008). The relatively low temperature and, consequently, the low diffusion rates of the gas phase in the melt (e.g. Zhang et al., 1991) strongly limits bubble resorption. Therefore, a scenario in which localization generates a connected gas network at different times and in different portions of the sample can reconcile rheological, FTIR and temperature data. This implies that, in our high pressure, isobaric experiments with a free surface intermittently connected to atmospheric pressure, degassing occurred in cycles and this process could eventually lead to a near complete degassing of magma. The extraction of gas from the melt phase is, in fact, a function of the final pressure at which the gas network is connected and the only limiting factor is the diffusion of the gas from the melt to the gas network.

(FIGURE 9)

Summary and implications

Experiments presented in this contribution corroborate the idea that deformation enhances bubble coalescence (e.g. Okumura et al., 2008; Okumura et al., 2009). The results also show that the residual water content of a deforming magma is not necessarily function of the confining pressure, but it could reflect the pressure at which an eventual gas network was connected (0.1 MPa in our experiments).

Our experiments show also that deformation in unsteady conditions produces flattening of bubbles, which, combined with coalescence, could generate gas-enriched

planar structures controlling the rheological behaviour of magma. Deformation in unsteady conditions is likely to occur in highly viscosity magmas (for a magma with viscosity 10^9 Pa·s, vesicles of 100 microns radius and surface tension of 0.25Nm^{-1} the bubble relaxation time is about 110 hours) and could play a role in the generation of banding often observed in obsidians (e.g. Castro et al., 2005; Gonnerman and Manga, 2003).

During ascent in a volcanic conduit, the release of gas from magma can occur via three main processes: 1) the formation of extended gas networks connected to lower pressure (shallower depths in the volcanic conduit), 2) the transition from viscous to brittle flow of magma, which would result in the generation of cracks with reduced pressure attracting the gas-phase (i.e. Tuffen et al., 2003; Tuffen and Dingwell, 2005), or 3) cracking of the volcanic conduit. The first process requires a significant length scale for the connected bubble network and evaluating its importance is not a trivial task. On the contrary, a plethora of field evidence exists for the second process (Tuffen et al., 2003; Tuffen and Dingwell, 2005). The third process has been documented by field observations of magmatic vents (Stasiuk et al., 1996), though shear stresses generated during magmatic flow along the conduit wall are not high enough to induce failure of the wall rocks (shear stress lower than 1 MPa for reasonable viscosity of the magma and dimension of the conduit; Stasiuk et al., 1996; Thomas et al., 2004). Nevertheless, along the conduit wall, where the strain suffered by magma is the largest, deformation could result in the generation of a connected gas network (Fig. 9B; e.g. Llewellin and Manga, 2005). If the pressure of the gas is higher than the confining pressure because of viscous retardation of bubble growth, which is typical for high viscosity magmas (Viscosity>10^9 Pa·s; Gonnerman and Manga, 2007), the pore pressure in the wall rock would increase, decreasing the

effective stress and eventually triggering extensional fracturing of the wall rocks (Terzaghi, 1945; Fig. 9). This mechanism could be a complementary process producing hybrid earthquakes during volcanic eruption (e.g. Tuffen et al., 2003).

An additional implication of the experimental results presented in this study regards the genesis of obsidians. Obsidians are generally depleted in water (Gottsmann and Dingwell, 2001, 2002; Rust et al., 2003; Castro et al., 2005) and contain very limited amount of crystals (Castro et al., 2002; Castro and Mercer, 2004). The possibility of continuous H_2O-degassing already at depth (i.e. from magmas with low bubble content) would reduce the amount of nucleation and growth of crystals (Hammer, 2008) during magma ascent. Additionally degassing will result in a substantial increase of viscosity, which would further inhibit crystallization (Dingwell and Webb, 1992; Dingwell, 1998). In conclusion strain-induced degassing could result in water under-saturation already in the early stages of magma ascent, reduce the tendency of the magma to crystallise and finally bring to the eruption of water and crystal poor magma, i.e. obsidians.

Figure Captions

Figure 1: Sketch of the experimental assembly used for the experiment. (B) Illustration of the possible path for gas-escape from the samples. The inset shows how gamma (γ) is calculated (Paterson and Olgaard, 2000).

Figure 2: (A-B) Variation of the applied shear stress as function of shear-strain. The maximum shear strain is γ =1.6 and γ =9.6 for (A) and (B) respectively. The picture in figure (A) is from the external portion of the experiment PP098 performed to a total γ of 2 using iron jacket. (C-D) Shear stress and temperature plotted against time. (C)

and (D) are enlargements of the regions marked by the dashed line in figure (A) and (B) respectively.

Figure 3: X-ray tomographic images of the starting material (A) and experiments PP116 deformed to γ 1.6 (B). The sketch of the sample in the inset shows the positions from where the samples for x-ray tomography were cut.

Figure 4: (A) 3D reconstructions of an internal section of the experiment PP117. This volume of sample underwent a deformation corresponding to γ 5.5 (Paterson and Olgaard, 2000). The arrows indicate the sense of shear. (B) Reconstructed volumes for experiment PP117. The tomographic scan was performed on the external portion of the sample where the total applied strain reached γ of 9.6.

Figure 5: Frequency distribution of bubble volumes expressed as equivalent radius (i.e. radius of a sphere with volume equal to the object under consideration) for the starting material and the sample deformed at different total strains.

Figure 6: Water content measured by FTIR for the starting material, a series of deformation experiment and for a static experiment performed at 100 MPa confining pressure 823 K for 10 hours. The error bar represents the variability of water content measured in 5 different points.

Figure 7: Logarithmic value of the apparent viscosity measured during the deformation experiments at different temperatures. The error bars for each data-point refer to the uncertainty associated to the presence of the metallic jacket and the resolution of the load cell (1Nm torque; Paterson and Olgaard, 2000). The lines are calculated values for the viscosity of melt containing 1.4 wt.% H_2O (black line) and the viscosity of melts containing 2 vol.% vesicles using Equation 2 (grey line). The data at 848 K represent most likely only upper values because at these conditions the iron jacket probably exerted a significant control on the measurements. These data are

presented to show the motivation behind their exclusion from the dataset used for the discussion on the rheological behaviour of the analysed samples.

Figure 8: Values of recorded stress during the experiment PP116 against strain. The sketches at the bottom of the figure represent the evolution of bubbles with increasing strain. The numbers in the sketches and in the diagram give the possible variations of stress associated to the evolution of the bubble with strain.

Figure 9: Possible evolution of the stress applied to the wall conduit during magma ascent and strain-induced magma degassing. The black line in the diagram represents a possible failure envelope for the rocks constituting the conduit wall. (A) The shear stress applied during magma ascent is not sufficient to fracture the conduit. (B) The higher shear stress and strain along the conduit wall could bring to bubble coalescence and the generation of a permeable gas network. The presence of gas would decrease the effective stresses (effective stress=stress-fluid pressure), applied by the magma rising in the conduit, and move the Mohr circle to lower stresses. (C) Once the gas pressure is high enough the Mohr circle reaches the failure envelope in the extensional field resulting in the generation of extensional fractures in the conduit wall.

Acknowledgements

This project was financed by an INSU grant and the Electrovolc project, which is funded by the French national agency for research (ANR): contract JC05-42707 to Fabrice Gaillard and by the NERC grant (NE/G012946/1) to Luca Caricchi. We are grateful to the local contacts Peter Modregger and Federica Marone at Swiss Light Source to make possible the x-ray tomography experiments and for their help with the 3D reconstructions and data treatment. The scientific discussions with

Fabrice Gaillard, Remi Champallier, Alison Rust and the technical support of Philip Teulat were greatly appreciated. The comments of Satoshi Okumura and two anonymous reviewers greatly improved the manuscript.

References

Castro, J., Manga, M., Cashman, K., (2002). Dynamics of obsidian flows inferred from microstructures: insights from microlite preferred orientations. Earth and Planetary Science Letters 199: 211-226.

Castro, J.M., Mercer, C., (2004). Microlite textures and volatile contents of obsidian from the Inyo volcanic chain, California. Geophysical Research Letters 31: doi:10.1029/2004GL020489.

Castro, J.M., Dingwell, D.B., (2009). Rapid ascent of rhyolitic magma at Chaiten volcano, Chile. Nature 461: 780-U729.

Castro, J.M., Manga, M., Martin, M.C., (2005). Vesiculation rates of obsidian domes inferred from H2O concentration profiles. Geophysical Research Letters 32: doi: 10.1029/2005GL024029.

Costa, A., Caricchi, L., Bagdassarov, N., (2009). A model for the rheology of particle-bearing suspensions and partially molten rocks. Geochemistry Geophysics Geosystems 10: doi:10.1029/2008GC002138.

Dingwell, D.B., (1998). The glass transition in hydrous granitic melts. Physics of the Earth and Planetary Interiors 107: 1-8.

Dingwell, D.B., Webb, S.L., (1992). The Fluxing Effect of Fluorine at Magmatic Temperatures (600-800-Degrees-C) - a Scanning Calorimetric Study. American Mineralogist 77: 30-33.

Gaillard, F., Scaillet, B., Pichavant, M., Beny, J.L., (2001). The effect of water and fO(2) on the ferric-ferrous ratio of silicic melts. Chemical Geology 174: 255-273.

Giordano, D., Russell, J.K., Dingwell, D.B., (2008). Viscosity of magmatic liquids: A model. Earth and Planetary Science Letters 271: 123-134.

Gonnerman, H.M., Manga, M., (2003). Flow banding in obsidians: A record of evolving textural heterogeneity during magma deformation. Earth and Planetary Science Letters 236: 135-147.

Gonnerman, H.M., Manga, M., (2007). The fluid mechanics inside a volcano. Annual Review of Fluid Mechanics 39: 321-356.

Gottsmann, J., Dingwell, D.B., (2001). The cooling of frontal flow ramps: a calorimetric study on the Rocche Rosse rhyolite flow, Lipari, Aeolian Islands, Italy. Terra Nova 13: 157-164.

Gottsmann, J., Dingwell, D.B., (2002). The thermal history of a spatter-fed lava flow: the 8-ka pantellerite flow of Mayor Island, New Zealand. Bulletin of Volcanology 64: 410-422.

Hammer, J.E., (2008). Experimental Studies of the Kinetics and Energetics of Magma Crystallization. Minerals, Inclusions and Volcanic Processes 69: 9-59.

Hashin, Z., Shtrikman, S., (1962). A Variational Approach to Theory of Effective Magnetic Permeability of Multiphase Materials. Journal of Applied Physics 33: 3125-3131.

Hess, K.U., Cordonnier, B., Lavallee, Y., Dingwell, D.B., (2008). Viscous heating in rhyolite: An in situ experimental determination. Earth and Planetary Science Letters 275: 121-126.

IAPWS (1997). Revised Release on the IAPS Formulation 1985 for the Viscosity of Ordinary Water Substance, International Association for the Properties of Water and Steam, Erlangen, Germany, 15.

Ketcham, R.A., (2005). Computational methods for quantitative analysis of three-dimensional features in geological specimens. Geosphere 1: 32-41.

Lensky, N.G., Lyakhovsky, V., Navon, O., (2001). Radial variations of melt viscosity around growing bubbles and gas overpressure in vesiculating magmas. Earth and Planetary Science Letters 186: 1-6.

Llewellin, E.W., Manga, A., (2005). Bubble suspension rheology and implications for conduit flow. Journal of Volcanology and Geothermal Research 143: 205-217.

Llewellin, E.W., Mader, H.M., Wilson, S.D.R., (2002). The rheology of a bubbly liquid. Proceedings of the Royal Society of London Series a-Mathematical Physical and Engineering Sciences 458: 987-1016.

Manga, M., Loewenberg, M., (2001). Viscosity of magmas containing highly deformable bubbles. Journal of Volcanology and Geothermal Research 105: 19-24.

Marziano, G.I., Schmidt, B.C., Dolfi, D., (2007). Equilibrium and disequilibrium degassing of a phonolitic melt (Vesuvius AD 79 "white pumice") simulated by decompression experiments. Journal of Volcanology and Geothermal Research 161: 151-164.

Moore, G., Vennemann, T., Carmichael, I.S.E., (1998). An empirical model for the solubility of H2O in magmas to 3 kilobars. American Mineralogist 83: 36-42.

Mysen, B.O., Yamashita, S., Chertkova, N., (2008). Solubility and solution mechanisms of NOH volatiles in silicate melts at high pressure and temperature-amine groups and hydrogen fugacity. American Mineralogist 93: 1760-1770.

Okumura, S., Nakamura, M., Tsuchiyama, A., Nakano, T., Uesugi, K., (2008). Evolution of bubble microstructure in sheared rhyolite: Formation of a channel-like bubble network. Journal of Geophysical Research-Solid Earth 113: 10.1029/2007JB005362, 2008.

Okumura, S., Nakamura, M., Takeuchi, S., Tsuchiyama, A., Nakano, T., Uesugi, K., (2009). Magma deformation may induce non-explosive volcanism via degassing through bubble networks. Earth and Planetary Science Letters 281: 267-274.

Paterson, M.S., Olgaard, D.L., (2000). Rock deformation tests to large shear strains in torsion. Journal of Structural Geology 22: 1341-1358.

Rolandi, G., Mastrolorenzo, G., Barrella, A.M., Borrelli, A., (1993). The Avellino Plinian Eruption of Somma-Vesuvius (3760 Y Bp) - the Progressive Evolution from Magmatic to Hydromagmatic Style. Journal of Volcanology and Geothermal Research 58: 67-88.

Rust, A.C., Manga, M., Cashman, K.V., (2003). Determining flow type, shear rate and shear stress in magmas from bubble shapes and orientations. Journal of Volcanology and Geothermal Research 122: 111-132.

Signorelli, S., Vaggelli, G., Romano, C., (1999). Pre-eruptive volatile (H2O, F, Cl and S) contents of phonolitic magmas feeding the 3550-year old Avellino eruption from Vesuvius, southern Italy. Journal of Volcanology and Geothermal Research 93: 237-256.

Stampanoni, M., Groso, A., Isenegger, A., Mikuljan, G., Chen, Q., Bertrand, A., Henein, S., Betemps, R., Frommherz, U., Bohler, P., Meister, D., Lange, M., Abela, R., (2006). Trends in synchrotron-based tomographic imaging: the SLS experience. Developments in X-Ray Tomography V 6318: U199-U212.

Stasiuk, M.V., Barclay, J., Carroll, M.R., Jaupart, C., Ratte, J.C., Sparks, R.S.J., Tait, S.R., (1996). Degassing during magma ascent in the Mule Creek vent (USA). Bulletin of Volcanology 58: 117-130.

Stein, D.J., Spera, F.J., (2002). Shear viscosity of rhyolite-vapor emulsions at magmatic temperatures by concentric cylinder rheometry. Journal of Volcanology and Geothermal Research 113: 243-258.

Terzaghi, K., (1945). Stress conditions for the failure of saturated concrete and rock. Proceedings American Society for Testing and Materials 45: 777-792.

Thomas, M.E., Petford, N., Bromhead, E.N., (2004). Volcanic rock-mass properties from Snowdonia and Tenerife: implications for volcano edifice strength. Journal of the Geological Society 161: 939-946.

Tuffen, H., Dingwell, D., (2005). Fault textures in volcanic conduits: evidence for seismic trigger mechanisms during silicic eruptions. Bulletin of Volcanology 67: 370-387.

Tuffen, H., Dingwell, D.B., Pinkerton, H., (2003). Repeated fracture and healing of silicic magma generate flow banding and earthquakes? Geology 31: 1089-1092.

Yoshimura, S., Nakamura, M., (2008). Diffusive dehydration and bubble resorption during open-system degassing of rhyolitic melts. Journal of Volcanology and Geothermal Research 178: 72-80.

Zhang, Y.X., Stolper, E.M., Wasserburg, G.J., (1991). Diffusion of Water in Rhyolitic Glasses. Geochimica Et Cosmochimica Acta 55: 441-456.

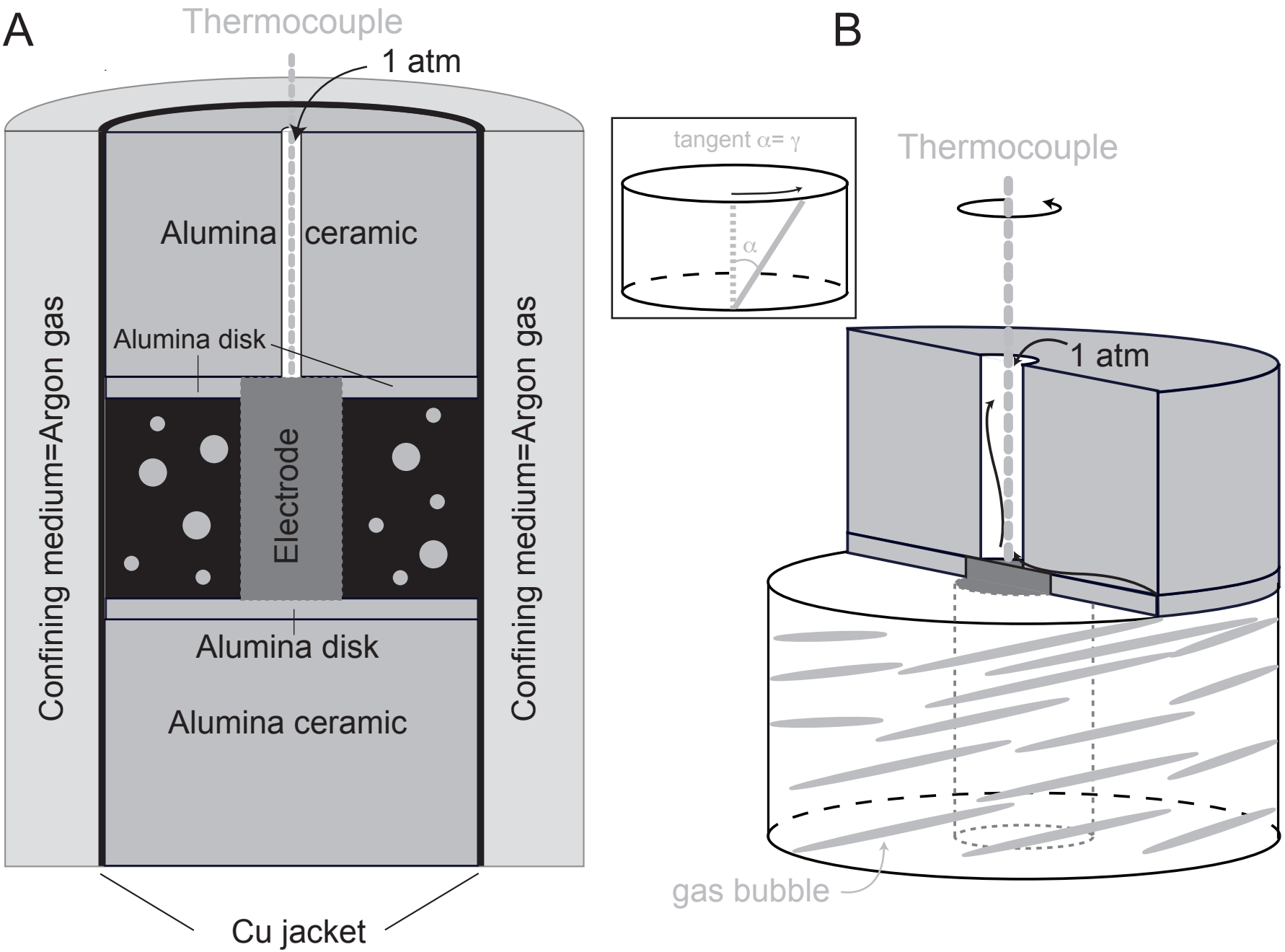

A
Thermocouple
1 atm
Alumina ceramic
Alumina disk
Electrode
Alumina disk
Alumina ceramic
Confining medium=Argon gas
Confining medium=Argon gas
Cu jacket
B
tangent α= γ
α
Thermocouple
1 atm
gas bubble

Figure 1

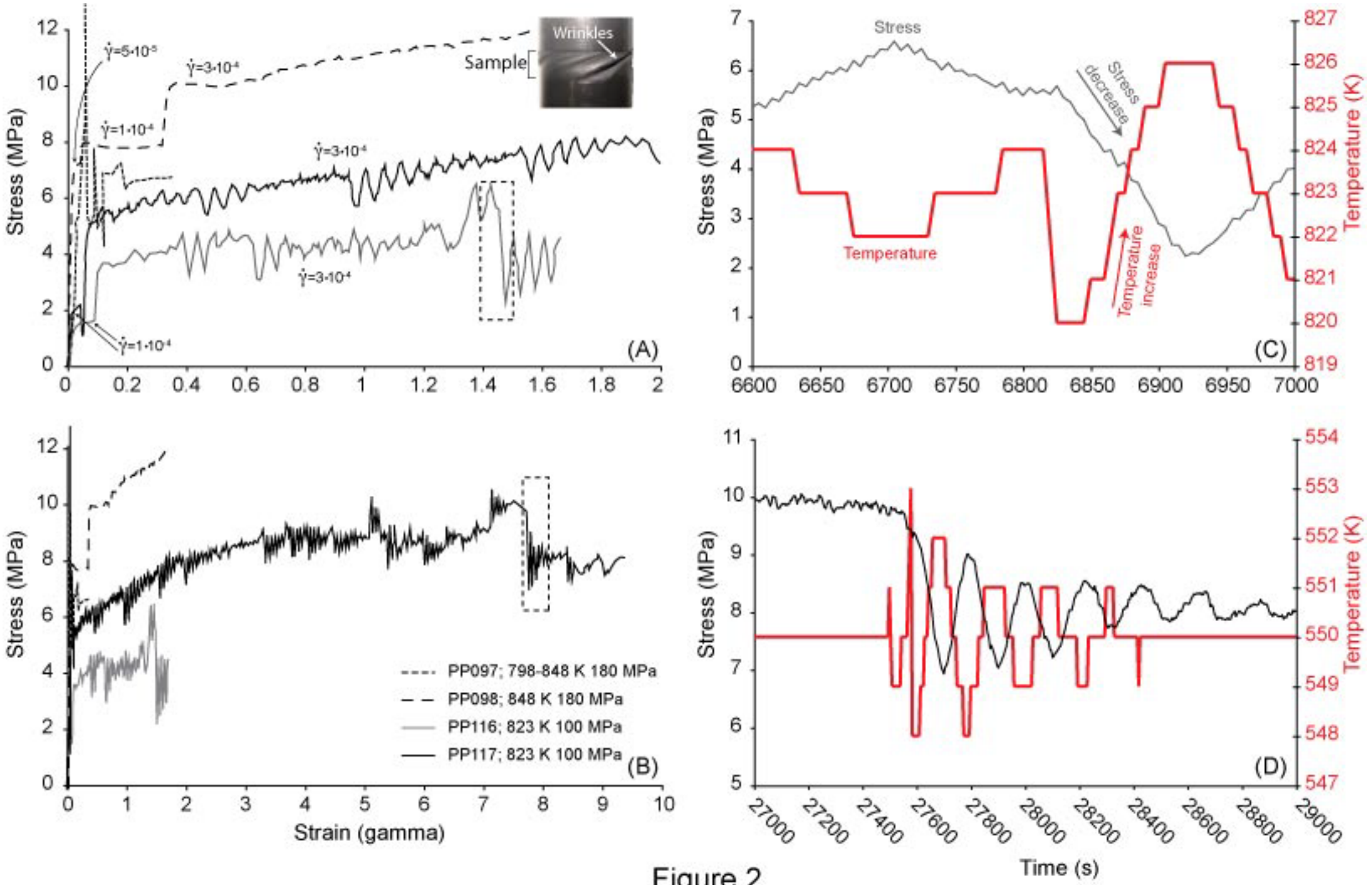

Stress (MPa)
Strain (gamma)
Time (s)
Temperature (K)
Wrinkles
Sample
$\dot{\gamma}$=5·10⁻⁵
$\dot{\gamma}$=3·10⁻⁴
$\dot{\gamma}$=1·10⁻⁴
$\dot{\gamma}$=3·10⁻⁴
$\dot{\gamma}$=3·10⁻⁴
$\dot{\gamma}$=1·10⁻⁴
(A)
PP097; 798-848 K 180 MPa
PP098; 848 K 180 MPa
PP116; 823 K 100 MPa
PP117; 823 K 100 MPa
(B)
Stress
Stress decrease
Temperature
Temperature increase
(C)
(D)

Figure 2

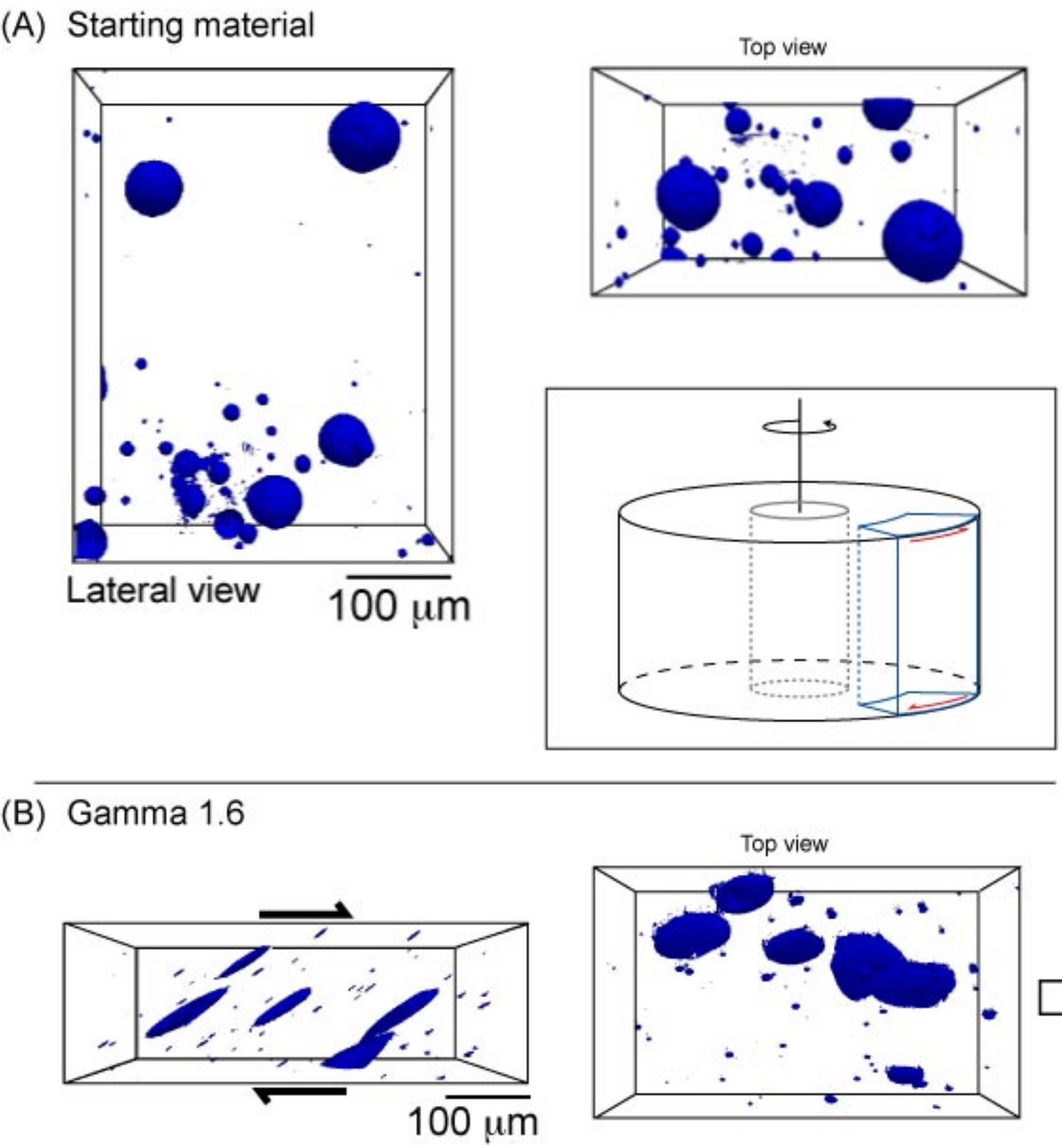
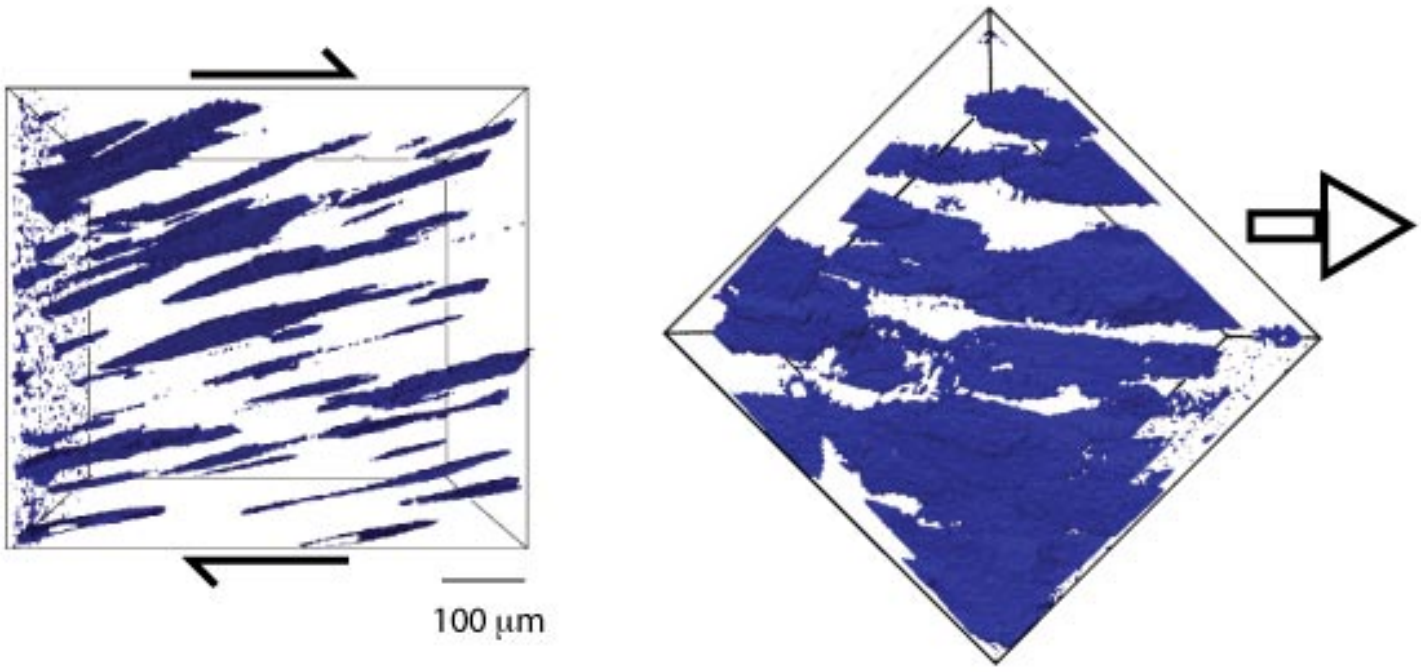

(A) Starting material
Top view
Lateral view
100 μm
(B) Gamma 1.6
Top view
100 μm

Figure 3

(A) Gamma 5.5



(B) Gamma 9.6

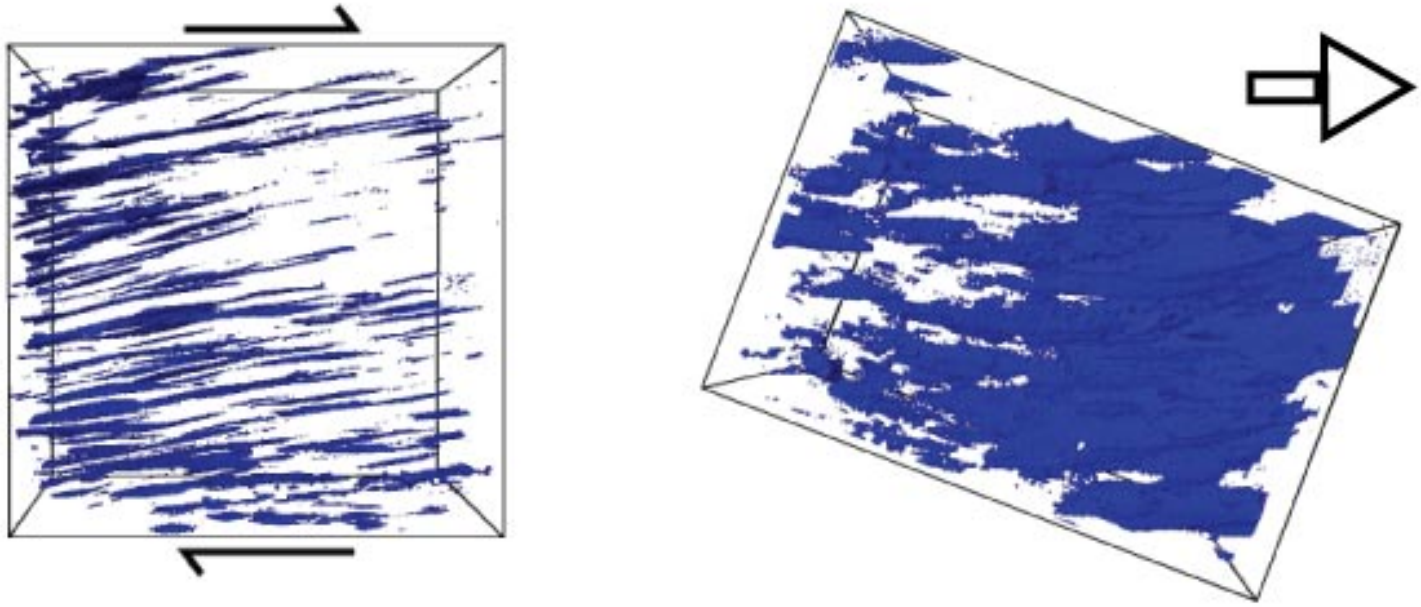


Figure 4

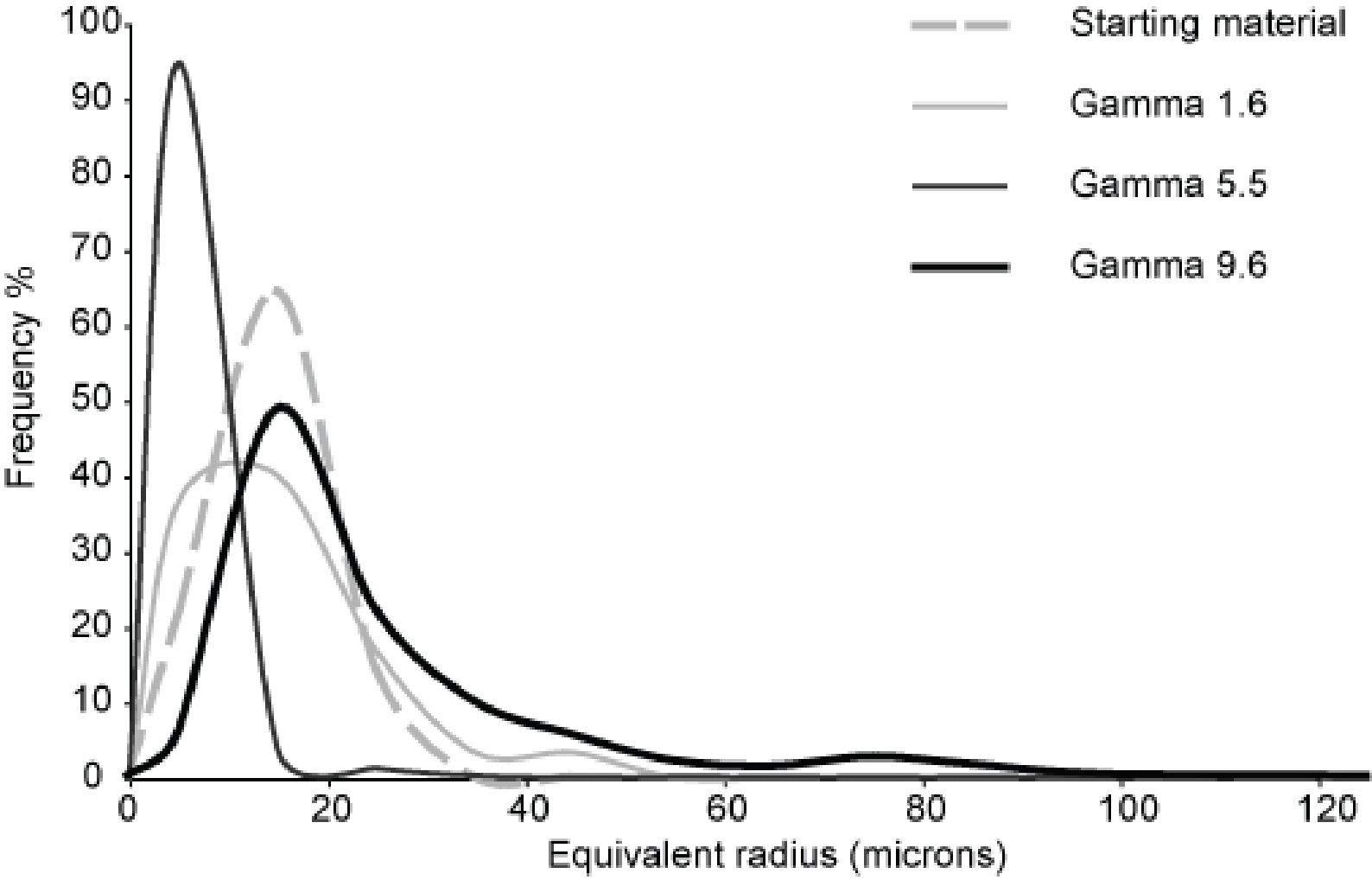

Starting material
Gamma 1.6
Gamma 5.5
Gamma 9.6
Frequency %
100
90
80
70
60
50
40
30
20
10
0
0
20
40
60
80
100
120
Equivalent radius (microns)

Figure 5

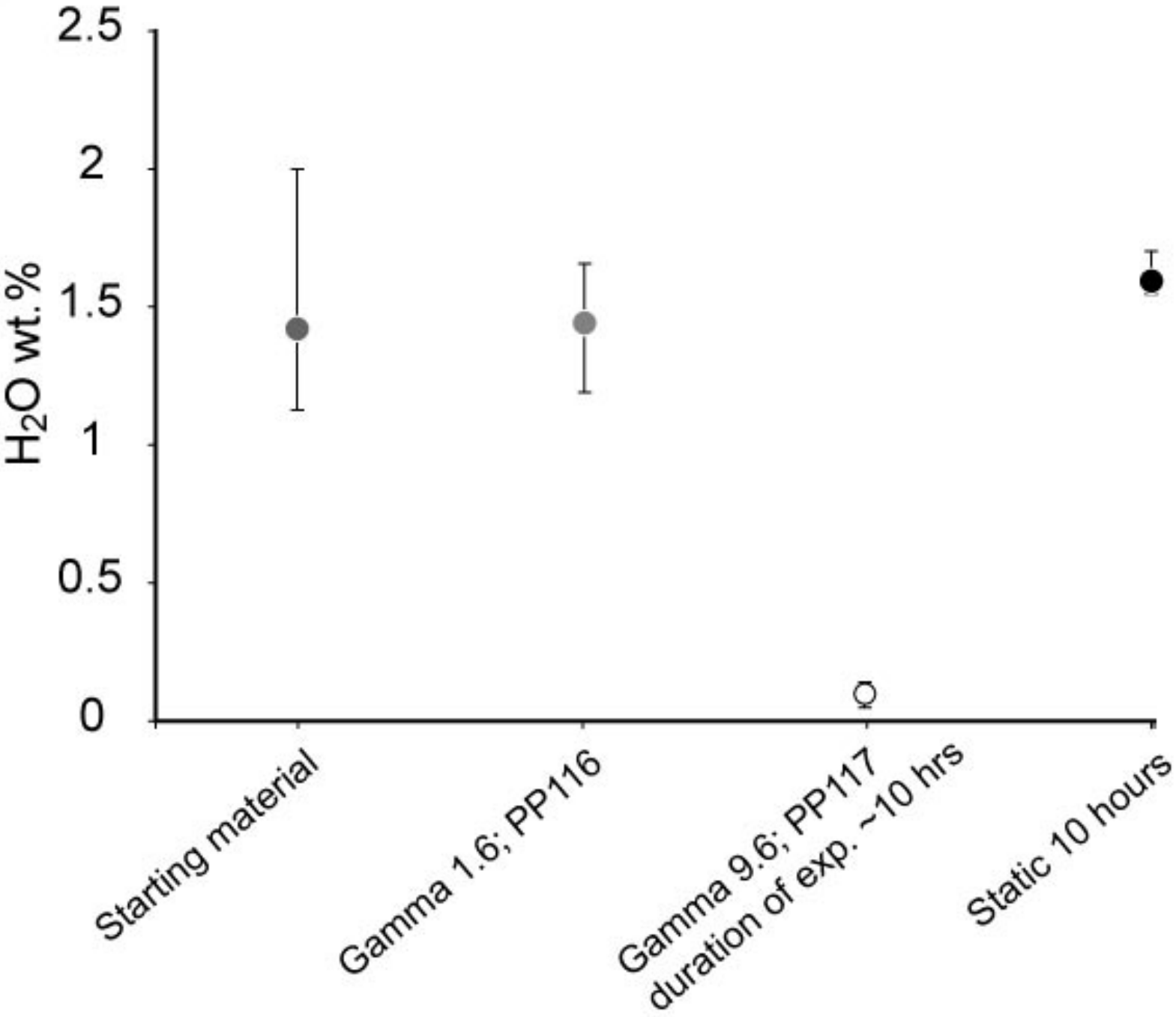

2.5
2
1.5
1
0.5
0
H2O wt.%
Starting material
Gamma 1.6; PP116
Gamma 9.6; PP117
duration of exp. ~10 hrs
Static 10 hours

Figure 6

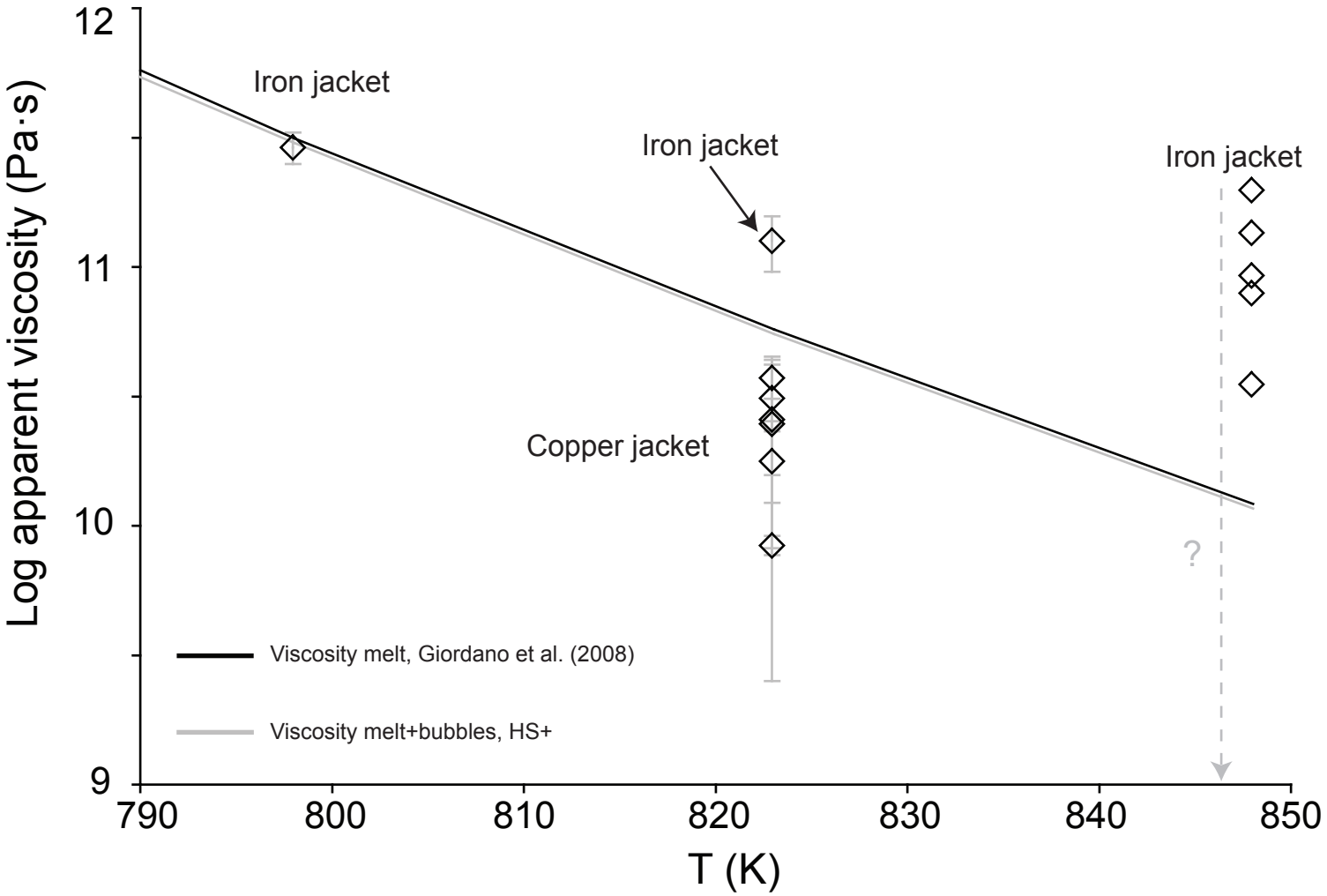

12
11
10
9
Log apparent viscosity (Pa·s)
790
800
810
820
830
840
850
T (K)
Iron jacket
Iron jacket
Iron jacket
Copper jacket
?
Viscosity melt, Giordano et al. (2008)
Viscosity melt+bubbles, HS+

Figure 7

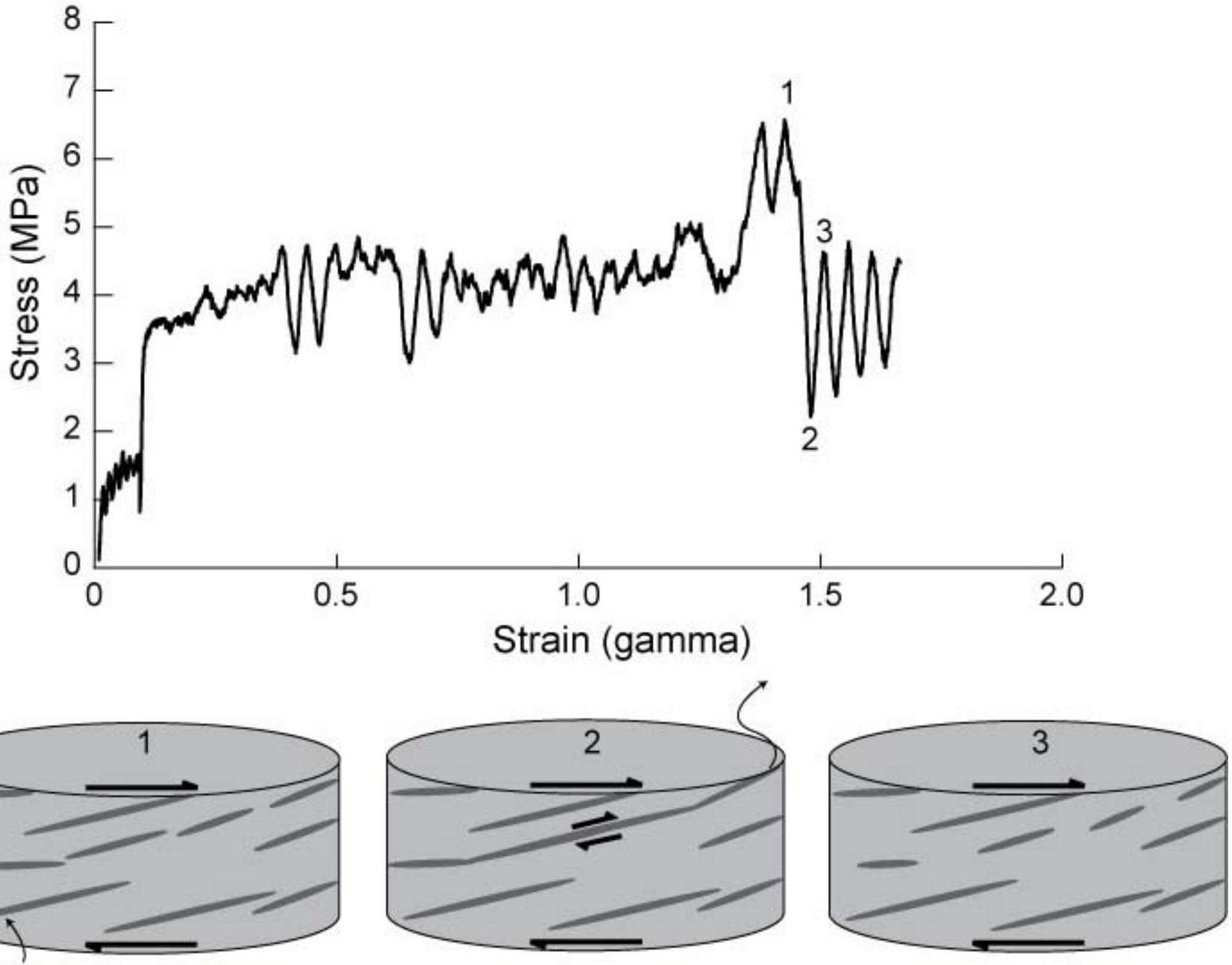

Stress (MPa)
0
1
2
3
4
5
6
7
8
0
0.5
1.0
1.5
2.0
Strain (gamma)
1
2
3
gas bubble

Figure 8

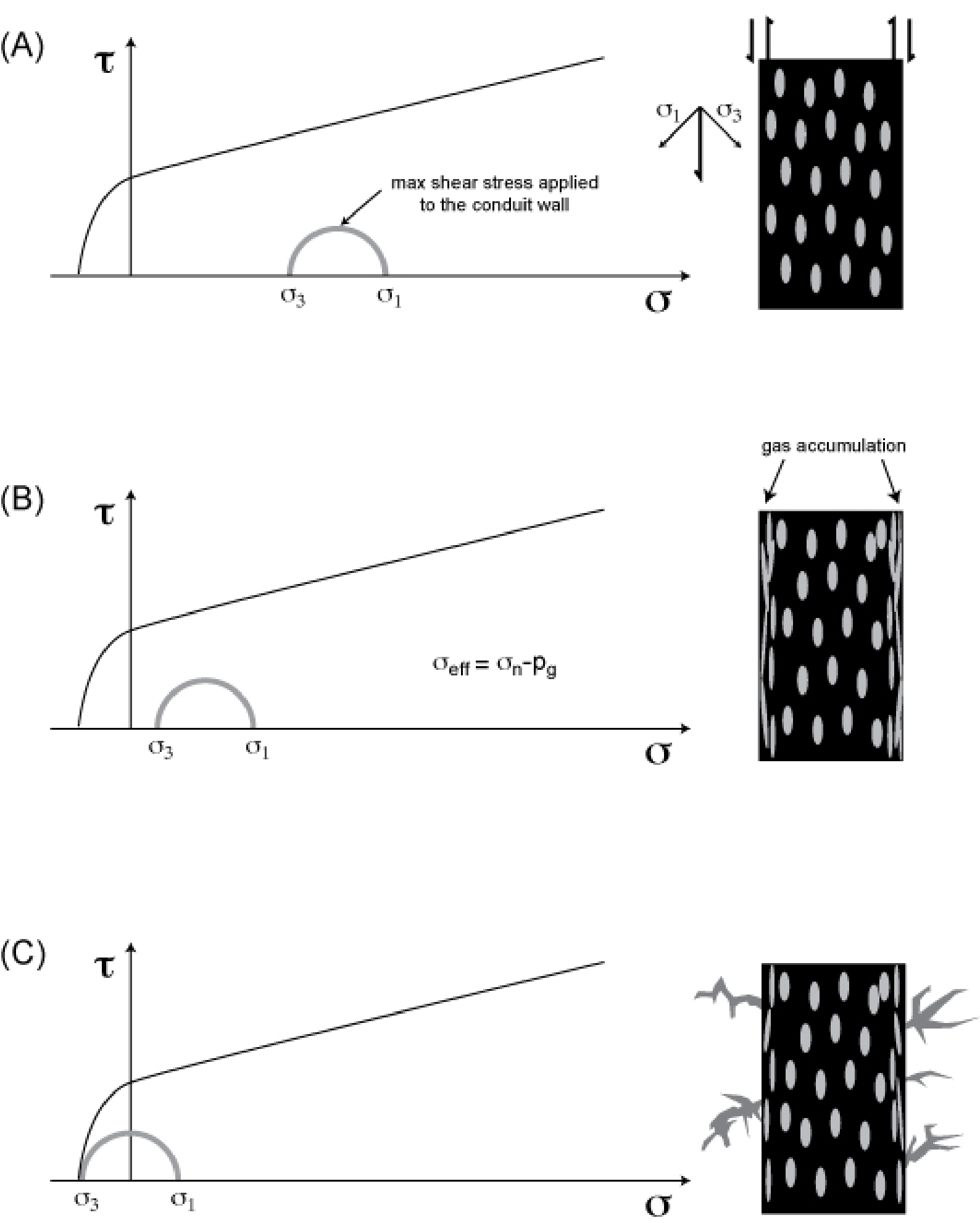

(A)
τ
σ
σ3
σ1
max shear stress applied
to the conduit wall
σ1
σ3
(B)
τ
σ
σ3
σ1
σeff = σn-pg
gas accumulation
(C)
τ
σ
σ3
σ1

Figure 9